

P04

## Pore-scale Single and Two-phase Transport in Real Porous Medium

I.I. Bogdanov\* (CHLOE, U. of Pau), J. Kpahou (CHLOE, U. of Pau) & F. Guerton (LFC-R, U. of Pau)

### SUMMARY

---

Since long time it has been recognized that the typical pore size is a fundamental scale in understanding of transport phenomena and determination of global transport properties of porous media. In a similar way like the Navier-Stokes equations may be used at certain limit to derive the Darcy law and define single phase transport properties, the modified Navier-Stokes model might be used to determine medium two-phase flow properties. Instead of using a regularization technique to capture the interface (cf. VOF or level-set functions approach), which may affect the modelling results in a non-trivial way, the diffuse interface method offers a thermodynamic treatment of phase “mixing” zone. As a result, it is a good choice for a numerical technique, handling the morphological changes of the interface which is of great importance for modelling of such a kind.

Like zero-order approximation which is at the same time the classical theory assumptions case, the two-phase flow properties (e.g. phase relative permeabilities) are simply two ultimate single phase flow configurations, one per each phase. In both cases only volumes occupied by one fluid are considered so that wetting and capillary properties becomes very important, probably along with the process history as they all are responsible for particular fluid distribution in pore space.

Taking advantage of recent advancements in X-ray computed micro-tomography ( $\mu$ CT), the reconstructed real porous medium samples (Bentheimer sandstone) are used for direct numerical simulations (DNS) of single and two-phase transport problems. Main model parameters - capillary, Reynolds, Cahn and Peclet numbers - are defined for each flow case. Emphasis is made on characterization of different steps and features of methodology based on  $\mu$ CT measurements, geometrical reconstruction, grid generation and computational models.

The contribution of DNS to understanding of transport phenomena in real media becomes increasingly important factor of porous medium description efforts.

## Introduction

The fast and continuous development of computer power, architecture and numerical models computational performance, gives rise to the problem formulations and solution approaches which until recently seemed to be inappropriate for practical use. Among them were direct numerical simulations (DNS) and/or measurements of flow in real pore space (cf. Bear 1988; chapter 1).

Currently the numerical simulations coupled with laboratory measurements get back more and more to the pore-scale description which is a fundamental approach in hydrodynamics. (We'll use hereafter a term "pore-scale" and not "micro-scale" to distinguish between them as the notion "microscopic point" defined, for instance, by Bear, 1988, refers to a REV scale containing by definition numerous pores). This approach is often addressed or mentioned when there is a need to improve our understanding of transport phenomena in such settings. It may provide valuable information about some principle theoretical notions underlying conventional flow models. In a similar way like the Navier-Stokes equations may be used at certain limit (low Reynolds number) to derive the Darcy law and define single phase transport properties, the generalized two-phase Navier-Stokes model (e.g. the diffuse interface approach, Cahn and Hilliard 1958, Badalassi et al. 2003) might be used to determine two-phase (and probably multi-phase) flow properties of a porous medium.

In particular the oil and gas production is highly depend on knowledge of key transport and storage properties of reservoir rock, such as porosity, absolute and phase relative permeabilities etc. The new approach which combines 3D rock sample imaging using micro-computed tomography ( $\mu$ CT) and direct numerical simulations (DNS), opens a way to evaluate pore volume geometry (and topology) and flow configurations in 3D space. In this paper a real Bentheimer sandstone sample is used to provide a virtual porous network. With this geometry, the pore-scale incompressible fluid flow model was used to calculate the macroscopic parameters of Darcy's law. An example of pore network of Bentheimer rock sample acquired via  $\mu$ CT is shown in Figure 1.

So the characterization of different steps and features of methodology based on  $\mu$ CT measurements, namely, the geometrical description of flow region via  $\mu$ CT reconstruction and imaging, the generation of a 3D grid in a real pore space, the discretized numerical model associated with this grid and the adequate flow computations, constitute the principal objectives of our current work. For the computation of fluid distribution inside pores, models based on incompressible Navier-Stokes equations and their extension to diffuse interface model (Cahn and Hilliard 1958) are used.

### Real porous medium: $\mu$ CT numerization

Interfacial phenomena occurring in multiphase flow in porous systems are strongly influenced by the geometric structure of rock porosity, so the precise geometrical characterization of void space in rock core sample becomes a key issue. The range of energies used in the X-ray tomography allows a study of very dense objects, such as rocks; moreover, the  $\mu$ CT technique gives a unique opportunity for non-destructive 3D core sample insight. The X-ray attenuation depends on the chemical composition of the material and its physical density. Resulting from improved software and measurements technique, the recent advances in X-ray  $\mu$ CT allowed greater access to both higher resolution and internal structure of core sample and to a larger set of information useful in the porous media flow modelling.

### *Acquisition*

For our study, a tomography device, Skyscan 1172  $\mu$ CT (by Bruker microCT), is used to analyse rock samples. The X-ray source (0.5 tungsten target, Hamamatsu) generates a polychromatic cone beam, in the X-ray wavelength range, whose spectral distribution allows the study of high X-ray attenuation media like a few millimeters thick rock samples. Prior to extract, via a dedicated image processing software, necessary data and the geometrical description of the connected porosities inside the sample, a tomographic acquisition of the latter has to be carried out. A well referenced rock, Bentheimer sandstone, has been investigated. A cylindrical 8 mm thick in diameter, 20 mm long plug

of this sandstone is shaped and fixed, inside the analysis chamber, on the appropriate stepping motor motorized holder, Figure 2 . This sandstone is mostly composed of consolidated silica grains. The space between silica grains constitutes the porous network. Some pores are partially filled by clays and feldspar.

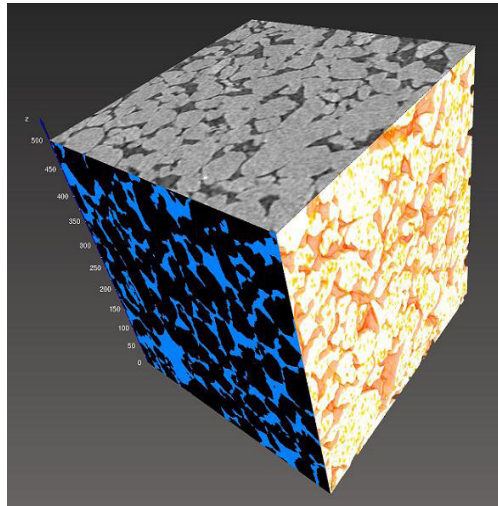


**Figure 1.** Bentheimer rock sample: raw reconstructed slice (upper face), sample texture (right face), segmentation (left face); side length  $L=2.45$  mm.

**Figure 2.** Bentheimer sandstone on the holder.

The sample's  $\mu$ CT acquisition is carried out in two steps. First, the apparatus records side view projections of the plug (2D radiographic greyscale images), one radiography (in plane parallel to the holder's rotation axis) per angular step. For this study a  $0^\circ$  to  $180^\circ$  total rotation,  $0.3^\circ$  angular step acquisition has been used (for calculation purposes, more than 600 projections are required). The beam emitted from the X-ray source get through the rock and the transmitted radiations are acquired via a  $4000 \times 2096$  pixels 12 bits camera (10 Mpixels, Hamamatsu). To improve the signal/noise ratio, each projection is the result of the image processing (dark and white fields correction, averaging, etc.) of 14 frames. Acquisition parameters are listed in Table 1. Inside the sample, X-ray's attenuation depends on the emitted radiation's wavelength, the chemical composition and the density of the materials encountered. In radiography, the greyscale (depicting the luminance) encodes the attenuation of the X-ray going through the object (the darker the pixel grey level, the higher the attenuation encounter by the beam inside the sample);  $4.9 \mu\text{m}$  per pixel has been chosen for the image resolution (set by the camera-object-source distances). Each frame takes about 2500 ms to be acquired (time exposition similar to classical optic photography). The exposition delay and the settings parameters (angle step, total rotation angle, number of frames used for the frame averaging, etc.) determine the total time for the analysis. For this study, the acquisition ran about 7 hours.



**Table 1.** Radiography parameters.

Side view	Resolution,	Angular	Total	Exposure,	Frames per
-----------	-------------	---------	-------	-----------	------------

image size, pixel	$\mu\text{m}$	step, degree	rotation degree	ms	step (#)
<b>4000×2096</b>	<b>4.9</b>	<b>0.3</b>	<b>0 → 180</b>	<b>2500</b>	<b>14</b>

On the second step, the recorded projections are processed via a Feldkamp-like algorithm to reconstruct, slice by slice, a virtual sample (Feldkamp et al. 1984). Contrary to a projection, a slice is an image which plane is perpendicular to the rotation axis: a projection is a side view, a slice a transversal view, Figure 3a. Each slice is a 16 bits TIFF format greyscale image (2D). This step is managed by the reconstruction software, NRecon, supplied with the Skyscan 1172 device. With no corrections, these images can be flawed: some artifacts inherent to tomography can damage the contrast, the structures' shape and boundaries inside the image. In addition, a built-in 0.5 mm thick aluminium + copper metal filter (apparatus' hardware option), is put between the camera and the sample. By this way the low energy part of the X-ray's energy distribution emitted by the source is attenuated, whereas the high energy part is kept almost unchanged. The slices can be loaded all in a one piece as a stack, which can be read as a volume (3D) depicting the sample acquired by tomography.

### *Pre-processing*

From the procedure described above, a stack composed of 500 slices of 500×500 pixels each, is obtained. This stack is read as a 500<sup>3</sup> voxels (voxel=volume pixel) virtual 3D sample. With a 4.9  $\mu\text{m}$  resolution, about 14.7 mm<sup>3</sup> is thus investigated for this study. At this stage, the volume is still coarse (composed of raw, noisy images). Prior to measure object's properties and extracting accurately the inner geometry, an image processing is required to improve the signal/noise ratio. Then, the result is segmented to separate porosities from the bulk (image binarization, see below). The software dedicated to open, process and visualize the virtual volume is Avizo (by VSG, Fire Edition). All the image processing steps are very sensitive to setting parameters; with a chosen well-documented Bentheimer rock we could control these image processing steps regarding to referenced values. Indeed, the whole image processing on the virtual sample leads to properties which can be compared with referenced data. Thus, a feedback can be easily obtained, and eventually the setting parameters been back adjusted.

The pre-processing of the stack is carried out as follow. The first goal is to increase the signal/noise ratio. To reach this result, 3D noise removing filters are successively applied on the volume. Firstly a *Median Filter* is used to remove salt-and-pepper type noise and high frequencies noises (Lim 1990). Then a *Bilateral Filter*, followed by an *Edge Preserving Diffusion Filter* are applied to lower medium-high to high frequency noises without appreciable boundaries' alterations, Tomasi and Manduchi (1998), Weickert et al. (1998). All these filters can be set-up: a good trade-off has to be found to get a satisfactory signal/noise ratio without altering edges and details too much. The outcomes of this filtering procedure are to emphasis the boundaries between porosities and the bulk, and the contrast between sample's components.

The second goal is to accurately discriminate porosities from bulk materials (*thresholding* or *segmentation*). Our case is in fact much easier, porosities (void space) have to be separated from the bulk (solid): only two materials have to be distinguished (binarization). For this purpose an automatic threshold filter, based on Otsu, Moments or Entropy algorithms, can be used (see Otsu 1979, Tsai 1985, Pun 1981 and Kapur 1985, resp.). Generally, automatic algorithms can only show a trend; manual adjustments have to be done to preserve as much as possible the geometry of the edges dividing porosities from the bulk. The result is binary encoded images, where "0" stands for porosities and "1" for materials. This operation, where only two phases have to be separated, is called binarization, Figure 3b. The porosity is computed from these binary slices according to a simple formula:  $(N_0/N_T) \times 100$  where  $N_0$  is the number of "0" encoded voxels, and  $N_T$  the total number of voxels. In literature, for Bentheimer sandstone, the mean porosity is  $0.21 \pm 0.006$  (experimental measurements), and may depend on the extraction's depth and the mineral deposit's location. A binarization quality criterion can be the accuracy of the transition boundary between the components

to be discriminated. Various settings parameters, in the noise filtering steps and the thresholding step, are investigated to get the best possible binarization. These trials lead to a mean and a standard deviation for the image processing porosity calculation,  $0.207 \pm 0.003$ . This result is in good agreement with the published experimental data. Nevertheless, in our case, mean and standard deviation are results of image processing trials of only one sample.

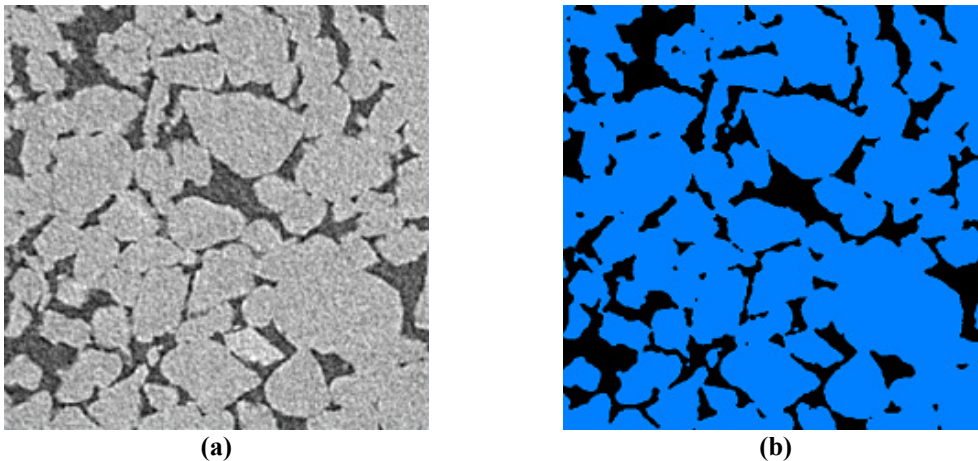


**Figure 3.** One raw slice of the sample (after reconstruction and cropping,  $500 \times 500$  pixels slice); pores are in the dark grey range, solid in the light grey range (a); image after noise filtering and binarization steps, black encodes pores, blue encodes solid (b).

### Geometrical description and image based grid generation

The objective of the previous image processing is to prepare the slices for being meshed using a dedicated software. Despite adequate noise filtering and *thresholding*, the stack is not ready to be meshed yet. Indeed, the procedure described in paragraph 3 cannot prevent the binarized stack from artefacts, due to inaccuracy of the segmentation process, like isolated floating aggregates in porosities, or isolated holes in the bulk. In the first case, these floating objects have no justification; in the second case, tiny holes in the bulk can be either segmentation artefacts or real unconnected porosities. Since these latter have no impact on the sample transport properties, they can be removed. If the volume is not processed to get rid of these isolated elements, the geometry of the object will be too much time and memory consuming for calculations.

#### *Morphologic filtering*

A morphologic filtering, is firstly applied on the stack: a hole-fill operation is carried out on the stack (hole-fill filter in Avizo Fire) to remove bubbles inside the bulk. Secondly, each element, inside the volume, is counted and measured (volume and area). From this measurement the elements can be sorted by size. One is much bigger compared to the others: the main bulk. Only this object is kept, thus floating aggregates in the porosities are removed. The binary stack is then code reversed (logical not operator): from this step “0” stands for the bulk and “1” for porosities. From now the objects depict the porosities. A *hole-fill* filtering, to close though-holes in the objects, followed by a size filtering, is applied on this new encoded stack. As result of these operations, only one object remains in the stack - the main connected porosity, Figure 4a.

This porosity (“1” coded voxels), can be meshed via a software specialized in surface or volume meshing providing a robust approach for the conversion of binarized or labeled stack images into surface or volume meshes (see Simpleware 2012). The generation of a mesh can be memory and time consuming regarding the computer’s efficiency. In order to reduce the total number of voxels to be handled for the meshing step, a data *resampling* or/and volume *cropping* can be performed on the stack (ScanIP tools). Isotropic *resampling* does not modify an object in size but reduced significantly

the total number of voxels. This operation may be somewhat critical because it modifies the connectivity, and hence the transport properties (by altering the pore network features and its shape, for example, weakly linked connections between pores may be removed etc.). We'll use hereinafter a term "resampled volume" to express the generated volume after *resampling* operation. The *cropping* is used to reduce the volume in size: a region of interest has to be chosen, in size and location, inside the stack. This cutting process can isolate some porous areas from the main network (indeed, new boundaries have been generated): the main network (connected porosities) has to be extracted from the new volume (defined as a region of interest), and the unconnected porosities removed.

A five iterations pre-smoothing, with the *part-change* option (ScanIP meshing tools), is applied on the stack prior to the meshing. Pre-smoothing is a topology and volume preserving algorithm. *Part-change* allows the surface to locally change to provide higher level of smoothing, but topology and volumes will still be preserved.

### *Unstructured grid generation*

The minimum *resampled* volume from original sample (of volume  $500^3$  voxels) maintaining the connectivity of the original rock sample is  $100^3$ . The total size of the object, however, does not change. To optimize the computational expenses, the  $100^3$  voxels *resampled* volume (of  $500^3$  voxels, initially) has been chosen as a sample for flow simulations. The calculated geometrical parameters of  $100^3$  voxels volume are presented in the Table 2 below. For each object a surface triangular mesh is to be generated first. Then the mesh is usually imported as geometry file into dedicated software (COMSOL 4.2a) for direct numerical simulations of pore-scale single- and two-phase (hereafter 1P and 2P, respectively) flow patterns.

One of the most important components for successful numerical pore-scale model (both in 1P and 2P cases) is an adequate choice of tetrahedral grid. As a rule the volume grid required rather fine discretization to get reliable results even for single-phase flow computations. By now all grids used in our work were generated with the use of local grid refinement towards grain surfaces ("*Fluid Dynamics*" built-in mesh generation option). Usually, the complicated geometry of pores and channels (Figures 4a,b) taken from reconstructed images without intermediate processing (smoothing), was prohibitive for generation of relatively coarse grid. One of smallest grid examples is shown in Figure 4b. It contains approximately  $2 \cdot 10^5$  of grid elements, the worst element quality being of order of 0.1. Typical examples of grid used in our study are presented in Table 3. Average discretization parameter is defined by equation (3) below. Grid generation has been performed on PC DELL containing 2 processors Intel(R) Xeon (R) X5650 @ 2.67 GHz, 8 CPUs, 96 Go of RAM.

**Table 2.** Geometrical parameters of  $100^3$  voxels resampled volume.

Volume, voxel	Total volume, m <sup>3</sup>	Connected pore volume, m <sup>3</sup>	Connected porosity, undim	Grain surface, m <sup>2</sup>	Typical pore size, m
<b>100<sup>3</sup></b>	<b>14.7e-9</b>	<b>2.75e-9</b>	<b>0.187</b>	<b>1.59e-4</b>	<b>68÷93e-6</b>

### **Single phase flow applications**

Single-phase flow transport properties may be computed first from steady-state 3D flow problem solution and then compared to experimental data. The flow models used in this study are dimensionless version of similar ones that can be found elsewhere (see Bogdanov et al. 2010).

#### *Model equations*

To obtain numerical results the incompressible Navier-Stokes (NS) model has been used. The dimensionless NS equations which may be written as

$$\begin{cases} Re \cdot \left( \frac{\partial \mathbf{u}}{\partial t} + (\mathbf{u} \cdot \nabla) \mathbf{u} \right) = -\nabla p + \nabla \cdot (\nabla \mathbf{u} + (\nabla \mathbf{u})^T) \\ \nabla \cdot \mathbf{u} = 0 \end{cases} \quad (1)$$

where

$$\mathbf{u} = u\vec{e}_x + v\vec{e}_y + w\vec{e}_z \quad (2)$$

$u, v, w$  local interstitial velocity components in  $x, y$  and  $z$  directions, respectively, describe laminar flow regime at Darcy limit (global Reynolds number meets  $Re \ll 1$ ). While the porosity computation is still straightforward and in principle available at earlier stage of image processing, the absolute permeability (or the total flow-rate through a sample) determination required more advanced procedure of flow simulation. It will generally depends on lateral boundary conditions (and so, on the sample shape) and discretization size. The roughness (or equally, smoothness) of grain surfaces which can hardly be measured at the moment, may be an important parameter together with 3D channels tortuosity. The latter can be modeled numerically basing on tomographic reconstruction images (Fourie et al. 2007 or Figure 5a below) and also measured experimentally using a known procedure.

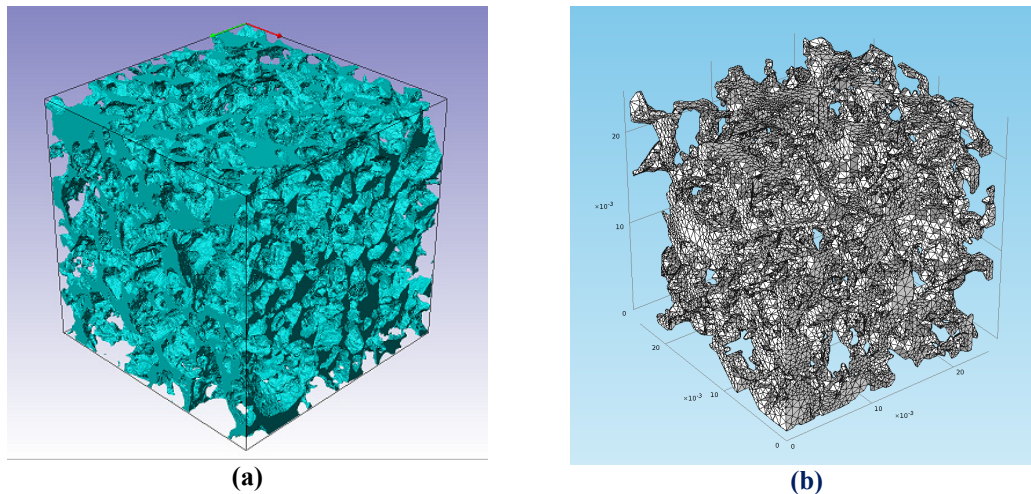


**Figure 4.** Numerized pore volume ready for mesh generation(a); one eighth of original Bentheimer sample: geometry and mesh;  $L_1=L/2$  (cf. Figure 1)(b).

**Table 3.** Grid examples for subsample 311.

Grid level	Min.element size, $\mu\text{m}$	Max.element size, $\mu\text{m}$	Max.element growth rate	Meshing time, s	Number of elements	Worst element quality	$D_{av}$ $\mu\text{m}$
normal	11.8	39.4	1.15	9.26	167371	0.2375	12.73
fine	5.88	31.2	1.13	12.26	237436	0.2611	11.32
finer	2.35	21.8	1.10	29.29	646048	0.2765	8.11
X fine	0.88	13.5	1.08	94.30	2087783	0.2892	5.49
XX fine	0.118	7.64	1.05	192.45	5282676	0.276	4.03

*Discretization and boundary conditions: impact on flow computations*

To evaluate the grid discretization and boundary conditions influence the subsample 311 (1/8<sup>th</sup> of original sample,  $L_1=L/2$ , Figure 4b) showing best isotropy of properties among all his counterparts,

has been chosen. Low enough Reynolds numbers can be controlled via imposed pressure drop between the inlet and outlet faces of a cubic sample. Special care has been taken to provide necessary mass balance in pore volume and laminar flow regime. Note that even at laminar flow conditions the local velocity field is far from being smooth and regular, Figure 5b; shown in the figure are velocities in the range  $2 \cdot 10^{-7} \div 6 \cdot 10^{-4}$  m/s). Different boundary conditions (BC) and grid discretization size ( $D_{av}$ , equation (3)) for all flow directions have been examined and their impact on a medium permeability was observed and documented.

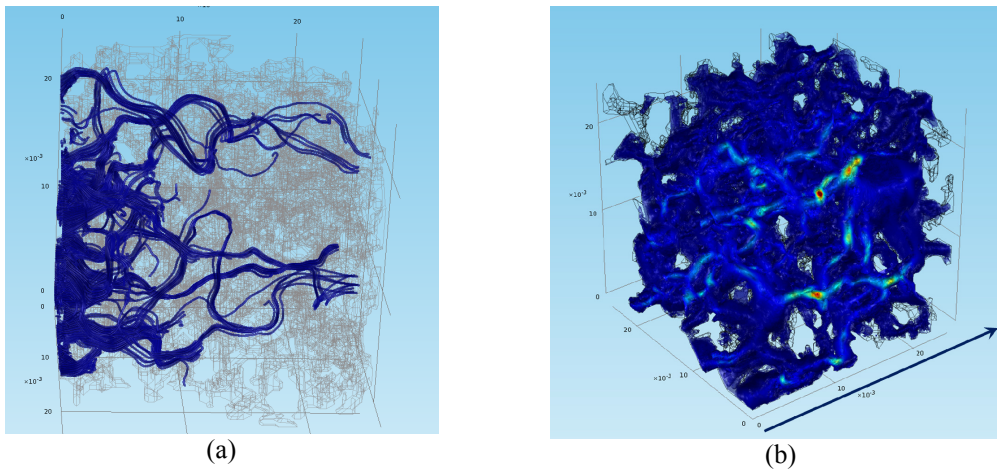


**Figure 5.** Streamlines of 1P stationary flow in 1/8th of original sample, flow direction is from left to right (a); local interstitial velocity field for the same case (b).

Figure 6 presents the directional permeability computations at different grid discretization. The discretization parameter  $D_{av}$  characterizing the average perfect tetrahedron side according to following relation

$$D_{av} = \sqrt[3]{\frac{(6 * \sqrt{2} * V_p)}{N_e}}, \tag{3}$$

has been used. Here  $N_e$  is the number of element and  $V_p$  is the pore volume. Coarse grid doesn't capture well the axial velocity profile and overestimate the resistance to flow in pores. Therefore the permeability is lower for greater discretization. Being solved formally with a FE of second order, the flow results demonstrate first order accuracy due to non-uniform grid, cf. Figure 4b. The estimation of true permeability value can be done after extrapolation at  $D_{av} \rightarrow 0$ . The results for different BC obtained for similar grid discretization include the no-slip, symmetry and periodic (2DP) lateral conditions, the inlet and outlet pressure being given for all these cases, Table 4. The 3D periodic BC were imposed using pressure difference conditions in the flow direction. Although the flow difference is relatively small, the results demonstrate regular flow-rate variation from no-slip to 3DP BC, the latter being less disturbing than others in a permeability estimation.

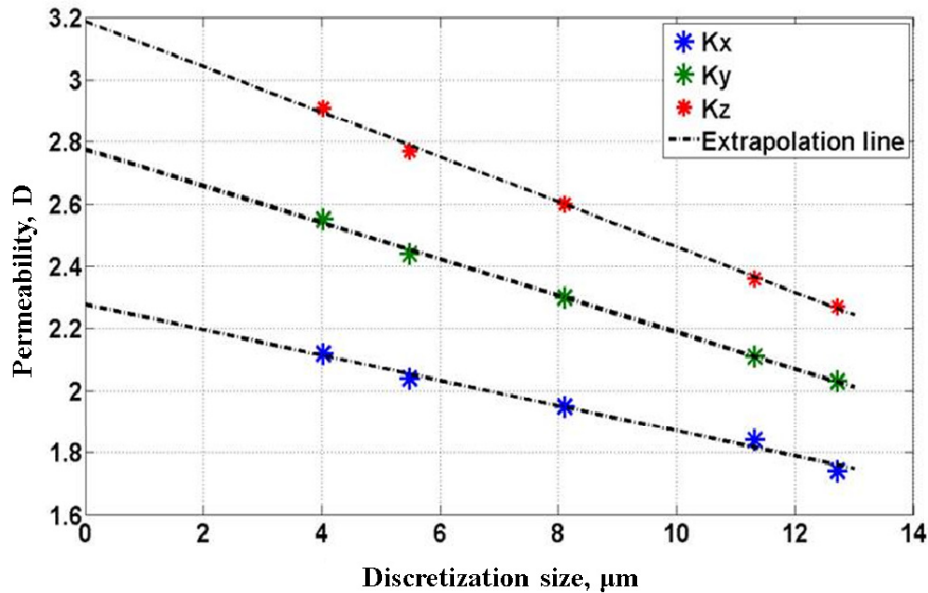


Figure 6. Variation of directional permeability with discretization size  $D_{av}$  (equation (3)).

Table 4. Impact of 1P flow boundary conditions on absolute permeability computations.

BC type	Flow direction	Inlet flowrate, $\text{m}^3/\text{s}$	Outlet flowrate, $\text{m}^3/\text{s}$	Permeability, D	Solution time
No-slip	X	5.68e-14	5.56e-14	1.83	63s
	Y	6.65e-14	6.95e-14	2.22	62s
	Z	7.96e-14	7.67e-14	2.49	60s
Symmetry	X	5.71e-14	5.59e-14	1.84	62s
	Y	7.05e-14	7.38e-14	2.35	58s
	Z	9.06e-14	8.91e-14	2.93	61s
2DP	X	2.28e-13	2.24e-13	1.84	312s
	Y	2.50e-13	2.70e-13	2.35	275s
	Z	3.61e-13	3.55e-13	2.92	259s
3DP	X	2.30e-13	2.30e-13	1.88	28min54s
	Y	2.97e-13	2.97e-13	2.42	27min17s
	Z	3.72e-13	3.72e-13	3.04	24min49s

### Two-phase flow applications

Numerically speaking, the technical problems in pore-scale simulations of two-phase flow arise mainly from the phase dynamic boundary (interface) modeling which is a problem of crucial importance for such an application. At the same time, available methods for modeling an interface separating fluids and possessing arbitrary configuration is strictly limited. Instead of applying a regularization technique to capture the interface, which may affect the results in non-trivial way, the diffuse interface method exploits a thermodynamic treatment of phase transition (or phase mixing) zone. As a result, physically justified approach is a good choice for a numerical technique, handling the morphological changes of the interface.

*Cand and Hilliard (1958) model*

The second gradient theory assumes that free energy of a system is a functional of an order parameter  $\varphi$ , its gradient  $\nabla\varphi$  and the temperature  $T$ . In the case of an isothermal binary fluid, a free energy can be defined for times when the system is not in equilibrium as:

$$F(\varphi, \nabla\varphi) = \int_{\Omega} \left[ \frac{1}{2} \alpha |\nabla\varphi(\mathbf{x})|^2 + G(\varphi) \right] d\mathbf{x} = \int_{\Omega} G_{tot} d\mathbf{x} \quad (4)$$

Here  $\Omega$  is the region of space occupied by the system and  $\varphi$  is a dimensionless phase-field variable which serves to identify the two fluids with volume fractions  $(1+\varphi)/2$  and  $(1-\varphi)/2$ . Accordingly the chemical potential is defined as:

$$\mu = \frac{\partial G_{tot}[\varphi(\mathbf{x})]}{\partial \varphi(\mathbf{x})} \quad (5)$$

The fourth order partial differential equation describing the evolution of  $\varphi$  is the convective Cahn-Hilliard (CH) equation:

$$\frac{\partial \varphi}{\partial t} + (\mathbf{u} \cdot \nabla) \varphi = \nabla \cdot [M(\varphi) \nabla \mu] \quad (6)$$

where the same notations like in equations (1,2) are used for dimensional variables (without loss of generality). For  $G$  a double potential form is chosen:

$$G(\varphi) = \frac{\alpha}{4\xi^2} (\varphi^2 - 1)^2 \quad (7)$$

where  $\alpha$  is the mixing energy density (N, cf. equation (4)) and  $\xi$  is a capillary width that scales with the thickness of the diffuse interface. Then the chemical potential is defined as

$$\mu(\varphi) = \frac{\partial G_{tot}(\varphi(\mathbf{x}))}{\partial \varphi(\mathbf{x})} = \alpha \left( -\nabla^2 \varphi + \frac{\varphi(\varphi^2 - 1)}{\xi^2} \right) \quad (8)$$

For the mobility  $M$  the expression chosen is:

$$M(\varphi) = M_c (1 - \gamma \varphi^2) \quad (9)$$

where  $0 \leq \gamma \leq 1$ . If  $\gamma \rightarrow 0$  then the phase separation dynamics is controlled by the bulk diffusion; if  $\gamma \rightarrow 1$  it is controlled by the interface diffusion. Thus the system of equations that we are going to solve:

$$\begin{cases} \mu(\varphi) = \alpha \left[ \frac{\varphi(\varphi^2 - 1)}{\xi^2} - \nabla^2 \varphi \right] \\ \frac{\partial \varphi}{\partial t} + (\mathbf{u} \cdot \nabla) \varphi = \nabla \cdot (M(\varphi) \nabla \mu) \end{cases} \quad (10)$$

The phase-field variable profile is obtained by minimizing the free-energy functional, with respect to variations of the function  $\varphi$ , i.e. solving:

$$\mu \equiv \frac{\delta F}{\delta \varphi} = \frac{\varphi(\varphi^2 - 1)}{\xi^2} - \nabla^2 \varphi = 0 \quad (11)$$

In the case of one-dimensional interface the solution is (Jacqmin 1999)

$$\varphi = \pm \tanh\left(\frac{z}{\sqrt{2}\xi}\right) \quad (12a)$$

The surface tension is equal to the integral of the free-energy density across the interface:

$$\sigma = \alpha \int \left(\frac{d\varphi(z)}{dz}\right)^2 dz \quad (12b)$$

Then the two parameters  $\sigma$  and  $\xi$  are linked through the relation

$$\sigma = \frac{2\sqrt{2}\alpha}{2\xi} \quad (12c)$$

### Spinodal decomposition

Like zero-order approximation which is at the same time the classical theory assumptions case, the two-phase flow properties (e.g. phase relative permeabilities) are simply two ultimate single phase flow configurations, one per each phase. In both cases only volumes occupied by one fluid are considered so that wetting and capillary properties becomes very important, probably along with the process history as they all are responsible for particular fluid distribution in pore space.

We begin the numerical experiments with an example of spinodal separation for a binary mixture in real porous medium. During decomposition uniformly disordered phases progressively separate into ordered structures and arrive at equilibrium with a minimum surface of the interface. At this state can be estimated the constitutive saturation-dependent relations underlying the classical theory of multiphase flow.

Let's take the Cahn-Hilliard equation describing this process normally without convection ( $\mathbf{u}(x)=0$ ) in its dimensionless form, i.e. as follows:

$$\begin{cases} \mu(\varphi) = \left[-\nabla^2\varphi + \frac{\varphi(\varphi^2 - 1)}{Cn^2}\right] \\ \frac{\partial\varphi}{\partial t} + (\mathbf{u} \cdot \nabla)\varphi = \frac{1}{Pe} \nabla \cdot (m(\varphi)\nabla\mu) \end{cases} \quad (13)$$

Here  $m(\varphi)$  is the dimensionless mobility coefficient

$$m(\varphi) = \frac{M(\varphi)}{M_c} = (1 - \gamma\varphi^2) \quad (14)$$

$Pe$  and  $Cn$  the Peclet and the Cahn number, respectively,

$$Pe = \frac{U_c L}{M_c \mu_c}, \quad Cn = \frac{\xi}{L} \quad (15)$$

The equations (13,14) completed with modified dimensionless NS equations

$$\begin{cases} Re \cdot \left(\frac{\partial\mathbf{u}}{\partial t} + (\mathbf{u} \cdot \nabla)\mathbf{u}\right) = -\nabla p + \nabla \cdot (\nabla\mathbf{u} + (\nabla\mathbf{u})^T) + \frac{1}{Ca} \mu \nabla\varphi \\ \nabla \cdot \mathbf{u} = 0 \end{cases} \quad (16)$$

where

$$Ca = \frac{\eta U_c}{\sigma}, \quad \sigma = \frac{2\sqrt{2}\alpha}{2\xi} \quad (17)$$

constitute finally the mathematical formulation of diffuse interface model (cf. Badalassi et al. 2003) or CHNS equations.

One example of the phase separation in case where there is no wetting phase (or in other words, the contact angle  $\theta=\pi/2$ ), is illustrated in Figures 7. Provided initial uniform perturbation of the form  $\phi_0=\varepsilon \cos(2\pi x/\delta)\cdot\cos(2\pi y/\delta)\cdot\cos(2\pi z/\delta)$ ,  $\varepsilon\ll 1$ , see Figure 7a, the decomposition process arrives at steady-state equilibrium with interface located mainly inside pore throats, Figure 7b. In this state the computation, for instance, of capillary pressure for given  $\sigma$  is straightforward.

*Example of a stable two- phase drainage*

Diffuse interface model of two-phase pore-scale mass transfer has been used for simulation of flow in real media. Viewed at micro-scale (i.e. REV-scale), the CHNS equations comprise at least 2 parameters to specify a “space” of possible flow regimes ( $Re \ll 1$  is fixed), namely, capillary number  $Ca$  (equation (17)) and viscosity ratio  $H=\eta_r/\eta_i$ , where subscripts “r” and “i” stand for recovered and injected fluids (typically, oil and water), respectively. Note also that the Cahn number (normally,  $Cn \ll 1$ ) and the Peclet number ( $Pe \gg 1$ , equation (15)) might contribute somewhat into flow pattern development.

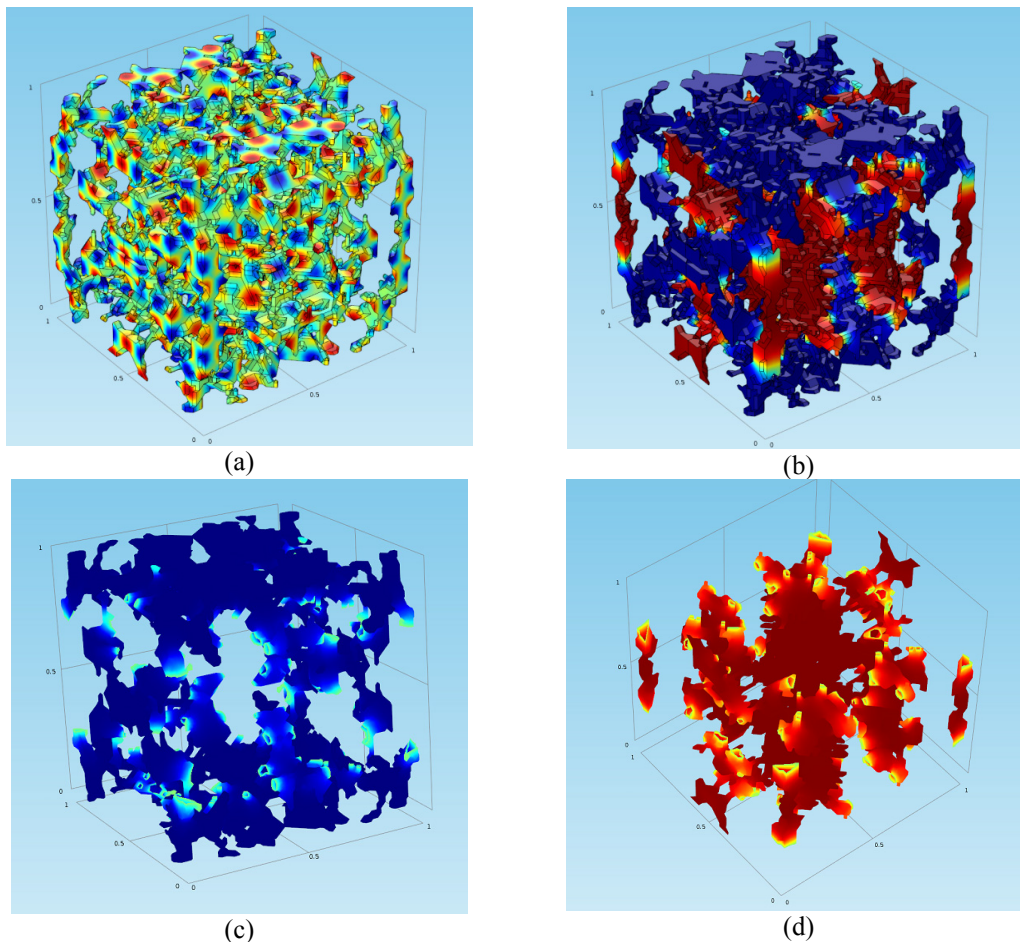


**Figure 7.** Red and blue phase decomposition at 3D periodic conditions: initial state,  $\varepsilon =0.1$ ,  $\delta=L/5$  (a); final (steady) state (b); state of each phase (c,d).

In particular, unfavorable viscosity ratio ( $H >1$ ) may lead to viscous fingering offset which is one of situations where multiscale analysis could be useful. The locally dominating capillary forces at pore scale are responsible for phase distribution in pores and capillary imbibition is an important transport mechanism at this scale. The use of realistic geometry of pores becomes evidently one of the key

factors in such a modelling. Recent example of stable 3D two-phase displacement without gravity in a real medium is shown in Figure 8. Even at  $H=0.1$  ( $Ca \approx 10^{-6}$ ), i.e. at stable displacement conditions, there is no flat displacement front at pore scale and each phase occupies its own space inside the pores. The pressure field demonstrates the local domination of capillary forces: the phase pressures vary only slightly over each phase volume, Figure 8d. At high enough capillary number the displacement becomes nearly discontinuous with distinct jump of interface over a pore followed by quasi-stationary very slow evolution. The capillary pressure can be evaluated straightforwardly from this type of numerical experiments.

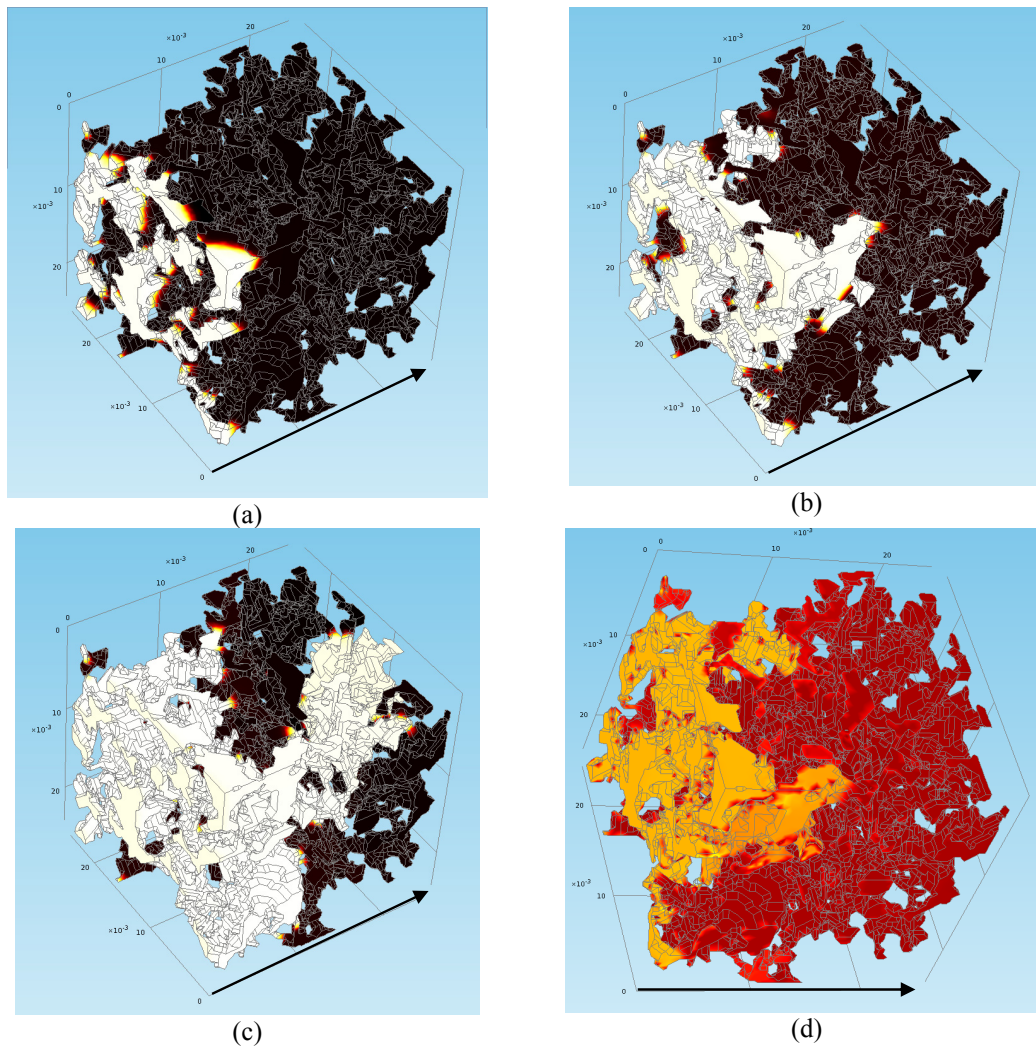


**Figure 8.** Fluids distribution for two-phase flow case at different time of displacement, the arrows indicate a global flow direction; the viscosity ratio is 0.1, the surface tension coefficient 0.01 N/m, the pressure difference 0.5 Pa. The volume fraction of injected liquid is equal to 6.7% (a), 28.9% (b) and 54.8% (c). Pressure distribution (d) corresponds to the same time as the order variable field (b).

## Conclusions

- Promising methodology combining of 3D  $\mu$ CT reconstruction and imaging of the real porous medium (Bentheimer sandstone, in the current study), the image processing for 3D pore volume geometry construction and finally, numerical mesh generation and flow simulations proved to result in a first 3D case study

- Both single- and two-phase flow in Bentheimer sandstone has been simulated using incompressible Navier-Stokes and Cahn-Hilliard diffuse interface models developed recently for 3D modeling of complex hydrodynamics
- Numerical evaluation of principal physical and geometrical characteristics and transport properties for single- and two-phase flow has been done previously for synthetic and now for real samples containing up to few hundreds pores
- The nearest future tasks embrace sensitivity studies of geometrical pore surface features and further computations of two-phase hydro-mechanical phenomena related to continuous and dispersed phase flow configurations and their petroleum applications

### Acknowledgement

TOTAL S.A. is gratefully acknowledged for sponsoring our research activities.

### References

Badalassi, V., Ceniceros, H., and Banerjee, S. [2003] Computation of multiphase system with phase field models, *Journal of Computational Physics*, **190**, 371-397.

Bear, J. [1988] *Dynamics of fluids in porous media*, Dover Publications, Inc., New York.

Bogdanov, I., Jardel, S., Turki, A., and Kamp, A. [2010] Pore-scale phase field model of two-phase flow in porous medium, *Proceedings of European COMSOL Conference*, Paris, France.

Cahn, J.W., Hilliard, J.E. [1958] Free Energy of a Nonuniform System. I. Interfacial Free Energy, *Journal of Chemical Physics*, **28**(2), 285-267.

Feldkamp, L.A., Davis, L.C., and Kress, J. W. [1984] Practical cone-beam algorithm, *Journal of the Optical Society of America A*, **1**, 612-619.

Fourie, W., Said, R., Young, Ph., Barnes, D.L. [2007] The Simulation of Pore Scale Fluid Flow with Real World Geometries Obtained from X-Ray Computed Tomography, *Proceedings of the Boston COMSOL Conference*, Boston, MA.

Jacqmin, D. [1999] Calculation of two-phase Navier–Stokes flows using phase-field modeling, *Journal of Computational Physics*, **155**, 96–127.

Kapur, J.N., Sahoo, P.K., and Wong, A.K.C. [1985] A New Method for Gray-Level Picture Thresholding Using the Entropy of the Histogram, *Computer Vision, Graphics and Image Processing*, **29**(3), 273-285.

Lim, J.S. [1990] *Two-Dimensional Signal and Image Processing*, Englewood Cliffs, NJ, Prentice Hall, 469-476.

Otsu, N. [1979] A Threshold Selection Method from Gray-Level Histograms, *IEEE Transactions on Systems, Man, and Cybernetics*, **9**(1), 62-66.

Pun, T. [1981] Entropic Thresholding: A New Approach, *Computer Graphics Image Process*, **16**, 210-239.

Simpleware [2012] *ScanIP +FE Module +CAD Module Reference Guide*, version 5.0

Tomasi, C., and Manduchi, R. [1998] Bilateral Filtering for Gray and Color Images, *Proceedings of the 1998 IEEE International Conference on Computer Vision*, Bombay, India.

Tsai, W. H. [1985] Moment-preserving Thresholding: A New Approach, *Computer Vision, Graphics, and Image Processing*, **29**, 377-393.

Weickert, J., Romeny, B.H., Viergever, M.A. [1998] Efficient and Reliable Schemes for Nonlinear Diffusion Filtering, *IEEE Transactions on Image Process*, **7**(3), 398-410.